Journal of
Applied Crystallography
ISSN 0021-8898

Received 16 August 2006
Accepted 31 October 2006

Development of an ultra-small-angle X-ray scattering instrument for probing the microstructure and the dynamics of soft matter

Michael Sztucki and Theyencheri Narayanan*

European Synchrotron Radiation Facility, BP 220, 38043 Grenoble, France. Correspondence e-mail: narayan@esrf.fr

A Bonse–Hart camera suitable for studying dilute and weakly scattering systems has been developed. The required level of reduction of the parasitic background scattering was realised by replacing channel-cut crystals by a pair of polished and deeply etched parallel crystals. The performance of this ultra-small-angle X-ray scattering instrument is illustrated by means of two examples: the microstructure of a short-range attractive colloidal system; and the growth dynamics of soot particles in a diffusion flame. In addition, the feasibility of performing dynamic X-ray scattering experiments is demonstrated.

1. Introduction

The Bonse–Hart camera has been widely used for (ultra) small-angle scattering experiments for more than 40 years (Bonse & Hart, 1965; Pedersen, 1995). The Bonse–Hart double-crystal set-up offers high angular resolution (limited mainly by the width of the rocking curve) and dynamic range of intensity (~8 orders of magnitude depending on the scattering power). At synchrotrons, ultra small-angle X-ray scattering (USAXS) has only been exploited since the advent of undulator sources (Diat *et al.*, 1995; Narayanan *et al.*, 2001; Ilavsky *et al.*, 2002). In the conventional pinhole SAXS camera, the angular resolution and intensity dynamic range are primarily restricted by the currently available two-dimensional detectors (Pontoni *et al.*, 2002; Gruner *et al.*, 2002). In addition, the typical beam divergence of an undulator source is comparable to the width of the reflectivity curves of Si-111 crystals. Therefore, the loss of intensity due to the finite acceptance of the crystals is less significant compared with laboratory X-ray sources. As a result, USAXS profiles can be recorded on reasonable time scales (minutes) at undulator beamlines (Narayanan *et al.*, 2001; Ilavsky *et al.*, 2002).

Despite advances in imaging methods, USAXS remains a very useful technique for obtaining bulk and ensemble averaged structural information at the micron range and below. Moreover, the scattering intensity, $I(q)$, is obtained on a quantitative scale which allows microscopic properties to be derived (which are otherwise inaccessible) using appropriate scattering models. As a result, USAXS is used to study multi-level structural features in nano-materials, microstructure and interactions in soft matter *etc.* (Long *et al.*, 1991; Pontoni *et al.*, 2003; Beaucage, Kammler, Mueller *et al.*, 2004; Beaucage, Kammler & Pratsinis, 2004; Narayanan *et al.*, 2006; Sztucki *et al.*, 2006). However, for probing micron scale structural information in crystalline and semicrystalline systems, a high-resolution pinhole SAXS camera with a two-dimensional detector has certain advantages (Yagi & Inoue, 2003; Petukhov *et al.*, 2006). The full scattering pattern is recorded simultaneously, whereas a Bonse–Hart camera requires sequential acquisition which could be a problem for oriented specimens and samples which are radiation sensitive. Accordingly, both methods are complementary and essential for recording SAXS over a wide dynamic range in scattering vector and intensity.

Bonse–Hart double-crystal diffractometers with multi-bounce channel-cut crystals show rocking curves which deviate considerably in their wings from the dynamical theory of diffraction (Agamalian *et al.*, 1998). This has adverse consequences for studying dilute and low-scattering samples as well as dynamic scattering.

This article presents a method to reduce this parasitic background. Many potential applications become feasible by improving the parasitic background and exploiting the coherent properties of the X-ray beam. Two representative examples involving dynamical processes in soft materials are presented. One deals with the microstructure of short-range attractive colloids, and the second involves growth dynamics in an extremely dilute system consisting of soot particles in an acetylene diffusion flame.

To exploit the improvement in the instrumentation, more efficient online processing of the acquired data is critical. For this purpose, a *Matlab*-based graphical user interface was developed. It allows direct evaluation and modelling of Bonse–Hart USAXS and pinhole SAXS data. Details of this graphical interface are provided in Appendix *A*.

2. Experimental set-up

Fig. 1 shows the schematic layout of a USAXS Bonse–Hart camera installed at the High Brilliance beamline (ID2) at the European Synchrotron Radiation Facility (ESRF) in Grenoble, France. The first triple-bounce Si-220 channel-cut crystal (monochromator) is crossed (orthogonal) with the Si-111 channel-cut monochromator of the beamline optics (not shown in the figure) and serves primarily for beam conditioning. The scattering intensity is analyzed by a set of two channel-cut crystals, a triple-bounce Si-220 horizontal crystal and an orthogonal double-reflection Si-111 vertical analyzer. The crossed configuration of the analyzer crystals eliminates the well known problem of desmearing of the double-crystal set-up, providing directly the high-resolution scattering profiles in point collimation. Two high dynamic range ($\sim 3 \times 10^7$ counts s^{-1}) avalanche photodiodes (APDs) operated in photon-counting mode record the incident and scattering intensities. Typically, a measured rocking curve spans more than 11 orders of magnitude in intensity. Fast pneumatically controlled attenuators are used to optimize automatically the count rates on the detector during a scan and also to protect the sample from radiation damage.

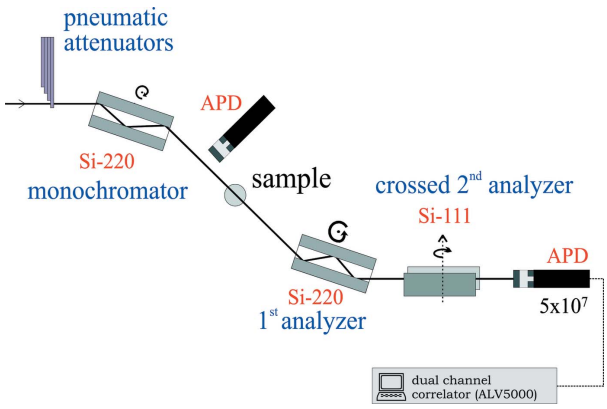

Figure 1
Schematic layout of the USAXS Bonse–Hart camera. The scattering intensity is measured by scanning the first analyzer crystal. The second analyzer is usually maintained at the Bragg angle. Two avalanche photodiodes (APDs) monitor the incident and scattering intensities. The incident intensity is recorded by measuring the scattering from a thin mica window which separates the vacuum in the incident section and sample stage.

The first analyzer crystal is rocked in linear or logarithmic steps to obtain the scattering profile as a function of the scattering vector, $q = (4\pi/\lambda)\sin(\theta/2)$, where λ is the incident wavelength and θ is the scattering angle. The second analyzer is usually maintained at the corresponding Bragg angle.

For typical static experiments, the central part of the rocking curve is measured in an initial linear scan which then continues in logarithmic steps to acquire the desired range of the scattering curve. As a result, the direct beam position, the width of the rocking curve and the transmitted intensity, I_T, are registered for each scan. This allows the measured intensity, $I_S(q)$, to be converted directly to an absolute scale [the differential scattering cross-section, $d\Sigma/d\Omega$ or $I(q)$] without requiring a calibration standard:

$$\frac{d\Sigma}{d\Omega} = \frac{I_S(q)}{I_0 A E T_r t \Delta\Omega} \qquad (1)$$

where I_0 is the incident flux, A the beam cross section, E the detector efficiency, T_r the sample transmission, t the known sample thickness, and $\Delta\Omega$ the solid angle defined by the rocking curves of the two analyzer crystals. $I_0 A E T_r = I_T$ is measured automatically for each scan; $\Delta\Omega$ is known from the widths of the horizontal and the vertical analyzer crystals. After normalizing by I_T, the scattering signal of the sample is superimposed on the normalized rocking curve without the sample. $I(q)$ of the sample can be obtained by a simple subtraction of the two normalized intensities, and then dividing by $\Delta\Omega$ and the sample thickness.

The Bonse–Hart camera installed at beamline ID2 is optimized to an operating energy of 12.4 keV. However, provision is made to operate up to 16 keV. The set-up provides a useful q-range of $10^{-3} < q < 1$ nm^{-1} at 12.4 keV ($\lambda \simeq 1$ Å). High quality rocking curves can be usually recorded within an acquisition time of a few minutes. The typical rocking curve width is about 14.5 µrad (full-width at half-maximum, see Fig. 2) and the scans are reproducible within about one µrad.

Optionally, the coherent part of the beam can be selected with a small slit setting (0.03 × 0.03 mm). In this configuration the parasitic scattering of the slits is effectively curtailed by the monochromator crystal. Dynamic X-ray scattering (DXS) or X-ray photon correlation spectroscopy (Abernathy *et al.*, 1998) can be performed by feeding the signals of the two APDs to an ALV 5000-E dual channel correlator. This provides the homodyne intensity–intensity autocorrelation function $g^{(2)}(q, t)$ for the scattering as well as the incident intensities. The $g^{(2)}(q, t)$ of the incident intensity is used as a baseline which is subtracted from the $g^{(2)}(q, t)$ of the sample. The resulting quantity is used to extract the dynamics in the sample under investigation.

3. Results and discussion

3.1. Reduction of parasitic scattering

Fig. 2 shows the improvement in the parasitic scattering background in the wings of the rocking curve obtained using two sets of polished and deeply etched flat crystals which are precisely aligned parallel to each other. For a comparison, the rocking curve obtained with a regular channel-cut crystal and the reflectivity curve calculated by the dynamical theory of diffraction using the program *XOP* (Sánchez del Río & Dejus, 1997) are shown. An improvement of more than one order of magnitude in the background is evident and it compares well with that observed in a neutron Bonse–Hart camera (Agamalian *et al.*, 1998). The residual background can be attributed to the mica windows in the set-up. Therefore, it is likely that the origin of the observed parasitic scattering background is a network of cracks in the surface of the crystals formed during fabrication. These cracks separate the surface layer of the crystal into small crystallites, which are slightly misoriented with respect to each other (Agamalian *et al.*, 1998). More details of the mechanical set-up and the X-ray performance will be reported elsewhere (Sztucki *et al.*, 2007).

This improved Bonse–Hart set-up has a lower scattering background than an optimized pinhole SAXS camera (q range 0.001–0.2 nm^{-1}) and thereby provides new opportunities for probing the structure and dynamics of soft matter in the ultra-small-angle range.

3.2. Microstructure and dynamics

Fig. 3 shows a representative example that demonstrates the usefulness of having a wide q range and a high dynamic range in $I(q)$ at the same time. The experimental system consists of stearyl silica particles in *n*-dodecane which interact *via* a short-ranged interparticle potential. The system undergoes a thermally reversible transition from repulsive hard spheres to attractive spheres by lowering the temperature T below a well defined value T_A (Narayanan *et al.*, 2006;

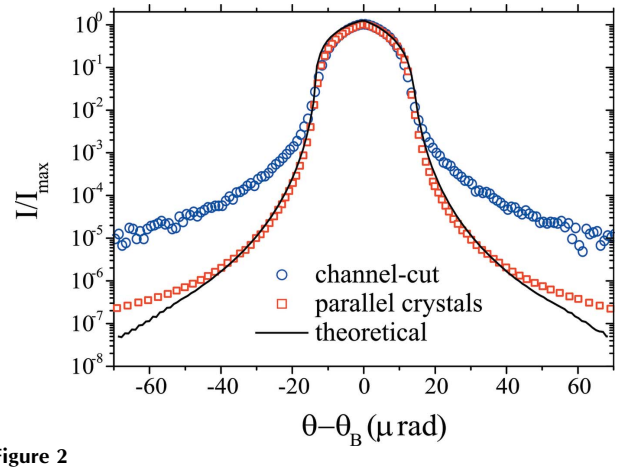

Figure 2
Comparison of rocking curves obtained using regular channel-cut crystals and mechanically fabricated devices, each consisting of two parallel polished and etched crystals. The parasitic scattering background in the wings of the rocking curve was suppressed by more than one order of magnitude using the latter set-up. The continuous line indicates the rocking curve calculated by the dynamical theory of diffraction. The curves are plotted relative to the Bragg angle, θ_B, of Si-220.

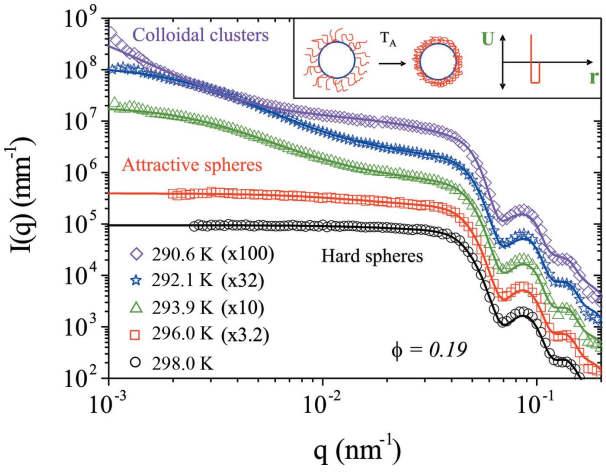

Figure 3
The evolution of the USAXS intensity in a short-range interacting colloidal system consisting of stearyl silica particles in *n*-dodecane upon cooling below T_A. The data demonstrate the transition from repulsive hard spheres to attractive spheres and the subsequent formation of colloidal clusters. For better visibility, the absolute $I(q)$ is multiplied by the factor indicated in the legend. The inset depicts schematically the transformation of the particles and the corresponding potential of interparticle interactions.

Sztucki *et al.*, 2006). The structure and dynamics of these short-ranged attractive colloids is a topic of contemporary interest (Dawson *et al.*, 2001; Sciortino & Tartaglia, 2005). This is a model system to verify the prediction by theory and computer simulations. Fig. 3 shows the evolution of the interactions for a sample of colloid, volume fraction $\phi \simeq 0.19$. As the short-range attraction is turned on by lowering the temperature below T_A, the system transforms from repulsive hard spheres to attractive spheres and then forms colloidal clusters. As schematically depicted in the inset, the transition corresponds to the development of an attractive square-well potential with a depth of several k_BT and a width comparable with the thickness of the stearyl layer, where k_B is the Boltzmann constant. The high q data show the oscillations from the particle form factor, whereas the intermediate q range is dominated by the structure factor of interaction. The low q upturn at lower temperatures is a clear indication of the formation of colloidal clusters. The total intensity can be described by

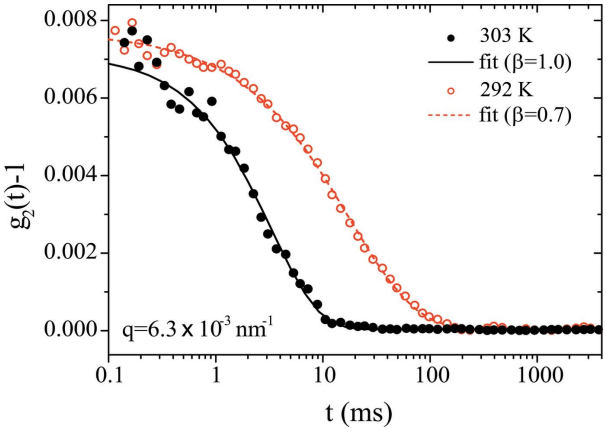

Figure 4
The intensity autocorrelation function $g^{(2)}(t)$ obtained from DXS for a sample with $\phi \simeq 0.12$. The functional form of $g^{(2)}(t)$ changes from single to stretched exponential behaviour when the particles become attractive.

$$I(q) = N_p \Delta\rho^2 V_p^2 P(q)\left[S(q) + S_c(q)\right] \quad (2)$$

where N_p the colloid number density, $\Delta\rho$ the scattering contrast between the particles and the suspending medium, and V_p the average particle volume. $P(q)$ is the polydisperse form factor describing the spherical shape of the particles. The interparticle interaction is described by the structure factor, $S(q)$, for a square-well system calculated using the leading order series expansion of the Percus–Yevick approximation (Dawson *et al.*, 2001; Narayanan *et al.*, 2006; Sztucki *et al.*, 2006). $S_c(q)$ describes the structure factor of the colloidal clusters (Pontoni *et al.*, 2003; Pontoni & Narayanan, 2003; Sztucki *et al.*, 2006). USAXS allows the separation of the contribution from changes in interparticle interaction and particle aggregation.

By exploiting the coherence of the beam, the microstructure and dynamics of the sample can be probed in a single experimental set-up. Fig. 4 shows the evolution of the particle dynamics when the system transforms from repulsive hard spheres to attractive spheres. In a purely diffusive system, $g^{(2)}(q, t)$ shows a single exponential decay, whereas it changes to a stretched exponential function when the particles become attractive corresponding to their constrained motion (Pontoni *et al.*, 2003). The evolution of $g^{(2)}(q, t)$ is described by the following general expression:

$$g^{(2)}(q, t) = 1 + g^{(2)}(q, 0)\exp[-2(t/\tau_s)^{\beta}] \quad (3)$$

with β the stretching exponent and τ_s the characteristic diffusion time of the particles.

Although the signal level is rather low due to limited coherence, useful information about the particle dynamics can be extracted. A significant reduction in the parasitic background is essential to derive a proper homodyne $g^{(2)}(q, t)$ at very low q values avoiding possible heterodyning effects.

3.3. Dilute system

The merit of a reduced background is demonstrated by another application dealing with a dilute system of soot particles in an acetylene flame ($\phi \sim 10^{-6}$). USAXS is a powerful technique to elucidate the multi-level structure (primary particles, their aggregates and agglomerates) of aerosol systems (Beaucage, Kammler, Mueller *et al.*, 2004; Beaucage, Kammler & Pratsinis, 2004). Moreover, soot formation due to incomplete combustion of the hydrocarbon fuel is an important issue in environmental science. The growth dynamics of soot can be a very complex process (Sorensen *et al.*, 1998) which is not fully understood. The key advantage of USAXS is that it is a non-intrusive technique compared with electron microscopy and is not influenced by optical emission from the flame, which is a severe problem in light scattering.

Fig. 5 presents the *in-situ* monitoring of particle aggregation as a function of the distance above the burner, which is equivalent to the kinetic time of the process. The nucleation and growth of the primary particles is more visible in the SAXS q range, while the aggregate size can be extracted only with the help of USAXS. The continuous line is a fit to the unified scattering function (Beaucage, Kammler, Mueller *et al.*, 2004; Beaucage, Kammler & Pratsinis, 2004) providing radii of gyration of ~33 nm for the primary particles and ~230 nm for aggregates with fractal dimension ~1.8. The full agglomerate scattering is beyond the USAXS q range.

4. Conclusion

A Bonse–Hart camera with low background has many potential new applications in the study of soft matter. This is demonstrated by two

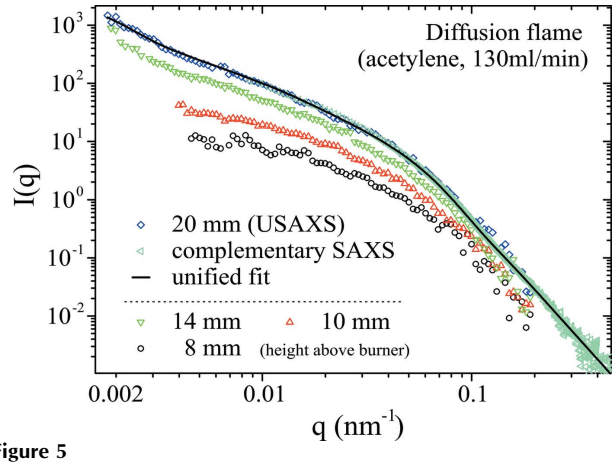

Figure 5
Comparison of Bonse–Hart USAXS and pinhole SAXS data for soot particles in a diffusion flame (acetylene, 130 ml min^{-1}, $\phi \sim 10^{-6}$) at different heights above the burner. Using the improved Bonse–Hart set-up, a considerable extension of the q range up to 0.0015 nm^{-1} could be obtained.

examples involving the microstructure and dynamics of a colloidal system, and the growth dynamics of soot particles in a diffusion flame. The microstructure and dynamics can be derived from the same experimental configuration. The improved set-up can be used for studying large biological complexes in the micron range.

APPENDIX *A*

A1. Online data processing and modelling

A *Matlab*-based graphical user interface has been developed for the online analysis of USAXS data taken with the Bonse–Hart set-up at beamline ID2 (see Fig. 6). From the initial linear scan (see Fig. 2), it automatically determines the transmitted intensity, I_T, and refines the centre of the measured rocking curve. Using the known $\Delta\Omega$, defined by the crossed analyzer configuration, the measured intensity is directly transformed to absolute units. The angular scale is automatically converted to the q scale in nm^{-1}. In addition, data files [format: two columns with q (nm^{-1}) and $I(q)$], for instance, recorded using the pinhole SAXS camera, can be imported. This allows a direct online comparison of SAXS and USAXS measurements.

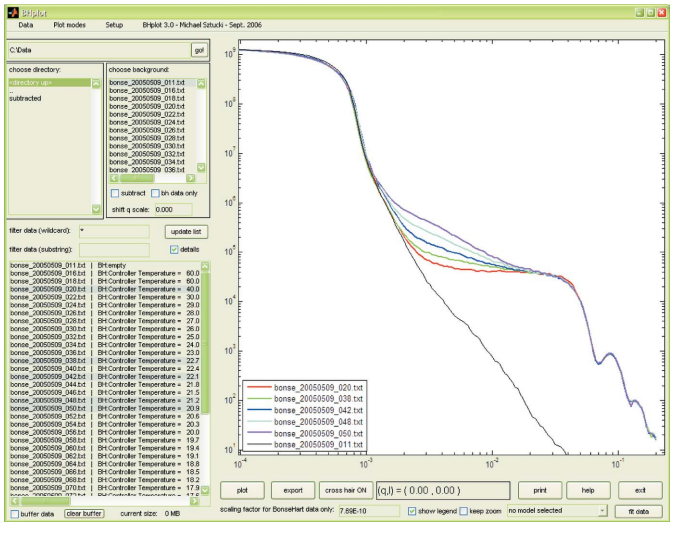

Figure 6
Matlab-based graphical user interface for online data processing and modelling of USAXS and SAXS data.

Different representations of the data are possible: double logarithmic, Guinier and Porod plots. A directory browser allows easy access to the data. Multiple data sets can be selected for simultaneous plotting. A background file can be selected from a separate listbox and can optionally be subtracted from all selected data files.

Furthermore, the possibility of online data modelling has been implemented. In separate graphical user interfaces the form factor of polydisperse spherical particles, core-shell particles and hollow shell can be fitted. Structure factor fitting of repulsive and short-range attractive hard spheres in Percus–Yevick approximation, as well as fitting of Debye–Bueche and fractal structure factors is available. The implementation of further models is planned and currently under development. The program is available in a compiled version (not requiring a *Matlab* licence) for Windows, Linux and Solaris.

We thank J. P. Vassalli and J. Härtwig in the optics group of the ESRF for the fabrication of the polished crystals, and L. Goirand, J. Gorini and P. van Vaerenbergh for engineering support. P. Bösecke, D. Fernandez, P. Panine and A. Sole are thanked for technical support and H. Hoekstra for providing the silica particles. The European Synchrotron Radiation Facility is acknowledged for financial support and the provision of beam time.

References

Abernathy, D. L., Grübel, G., Brauer, S., McNulty, I., Stephenson, G. B., Mochrie, S. G. J., Sandy, A. R., Mulders, N. & Sutton, M. (1998). *J. Synchrotron Rad.* **5**, 37–47.
Agamalian, M., Christen, D. K., Drews, A. R., Glinka, C. J., Matsuoka, M. & Wignall, G. D. (1998). *J. Appl. Cryst.* **31**, 235–240.
Beaucage, G., Kammler, H. K., Mueller, R., Strobel, R., Agashe, N., Pratsinis, S. E. & Narayanan, T. (2004). *Nature Mater.* **3**, 370–374.
Beaucage, G., Kammler, H. K. & Pratsinis, S. E. (2004). *J. Appl. Cryst.* **37**, 523–535.
Bonse, U. & Hart, M. (1965). *Appl. Phys. Lett.* **7**, 238–240.
Dawson, K. A., Foffi, G., Fuchs, M., Goetze, W., Sciortino, F., Sperl, M., Tartaglia, P., Voigtmann, T. & Zaccarelli, E. (2001). *Phys. Rev. E*, **63**, 011401.
Diat, O., Bösecke, P., Ferrero, C., Freund, A. K., Lambard, J. & Heintzmann, R. (1995). *Nucl. Instrum. Methods Phys. Res. A*, **356**, 566–572.
Gruner, S. M., Tate, M. W. & Eikenberry, E. F. (2002). *Rev. Sci. Instrum.* **73**, 2815–2842.
Ilavsky, J., Allen, A. J., Long, G. G. & Jemian, P. R. (2002). *Rev. Sci. Instrum.* **73**, 1660–1662.
Long, G. G., Jemian, P. R., Weertman, J. R., Black, D. R., Burdette, H. E. & Spal, R. (1991). *J. Appl. Cryst.* **24**, 30–37.
Narayanan, T., Diat, O. & Bösecke. P. (2001). *Nucl. Instrum. Methods Phys. Res. A*, **467**, 1005–1009.
Narayanan, T., Sztucki, M., Belina, G. & Pignon, F. (2006). *Phys. Rev. Lett.* **96**, 188301.
Pedersen, J. S. (1995). *Modern Aspects of Small Angle Scattering*, edited by H. Brumberger, p. 57. Dordrecht: Kluwer Academic Publishers.
Petukhov, A. V., Thijssen, J. H. J., 't Hart, D. C., Imhof, A., van Blaaderen, A., Dolbnya, I. P., Snigirev, A., Moussaïd, A. & Snigireva, I. (2006). *J. Appl. Cryst.* **39**, 137–144.
Pontoni, D. & Narayanan, T. (2003). *J. Appl. Cryst.* **36**, 787–790.
Pontoni, D., Narayanan, T., Petit, J.-M., Grübel, G. & Beysens, D. (2003). *Phys. Rev. Lett.* **96**, 258301.
Pontoni, D., Narayanan, T. & Rennie, A. R. (2002). *J. Appl. Cryst.* **35**, 207–211.
Sánchez del Río, M. & Dejus, R. J. (1997). *SPIE Proceedings*, **3152**, 148–157.
Sciortino, F. & Tartaglia, P. (2005). *Adv. Phys.* **54**, 471–524.
Sorensen, C. M., Hageman, W. B., Rush, T. J., Huang, H. & Oh, C. (1998). *Phys. Rev. Lett.* **80**, 1782–1785.
Sztucki, M., Gorini, J., Goirand, L., van Vaerenbergh, P., Vassalli, J. P., Härtwig, J. & Narayanan, T. (2007). *J. Synchrotron Rad.* In preparation.
Sztucki, M., Narayanan, T., Belina, G., Moussaïd, A., Pignon, F. & Hoekstra, H. (2006). *Phys. Rev. E*, **74**, 051504.
Yagi, N. & Inoue, K. (2003). *J. Appl. Cryst.* **36**, 783–786.